

First-principles investigation of stress effects on electronic, optical, elastic, and thermodynamic properties of cubic HfMgO₃ perovskite

M. USMAN MUSHTAQ¹, M. SANA ULLAH SAHAR², S. M. JUNAID ZAIDI³, MUHAMMAD BILAL⁴, MUHAMMAD HASHIM⁴, BASSEM F. FELEMBAN⁵, HAFIZ TAUQEER ALI⁵, M. IJAZ KHAN^{6,*}

¹Mechanical department, King Fahd University of Petroleum and Minerals, Kingdom of Saudi Arabia

²Department of Mechanical Engineering, University of Sargodha, Sargodha - 40100, Pakistan

³Department of Physics and Mathematics, Faculty of Sciences, Superior University, Lahore 54000, Pakistan

⁴Institute of Physics, The Islamia University, Bahawalpur, Pakistan

⁵Department of Mechanical Engineering, College of Engineering, Taif University, Taif, Kingdom of Saudi Arabia

⁶Institute of Mechanical and Manufacturing Engineering, Khwaja Fareed UEIT, Rahim Yar Khan, 64200, Pakistan

Due to its peculiar properties, perovskite oxide, a captivating class of perovskite materials, has drawn considerable interest from the scientific community in a variety of domains. A supercell of cubic morphological Hafnium Magnesium Oxide (HfMgO₃) was constructed utilizing a DFT methodology with an approximation of PBE-GGA in the CASTEP setting. The main objective of this work was to investigate how varied stress (0–160 GPa) affected the electrical, optical, elastic, mechanical, and thermal properties. Results show that a decline in the lattice parameter and the unit cell volume is seen. Additionally, the optical study illustrates how the band gap has changed as 0.442, 0.757, 0.734, 0.673, and 0.589 by applying stress 0, 40, 80, 120, and 160 GPa. Stress affects optical behavior, as seen by high absorption and conductivity, low loss function, and poor reflectivity, among other optical features. In the present work, the elastic constants and other mechanical parameters were scrutinized. According to calculated ratios like (Poisson's and Frantsevich), the material has a ductile character and anisotropy. These comprehensive findings will be helpful to open new avenues for experimental researchers and will contribute to a more profound indulgence of the effects of stress on perovskite oxides.

(Received March 26, 2024; accepted February 3, 2025)

Keywords: Band gap, Stress, Perovskites, Thermodynamic properties, First-principles calculation

1. Introduction

Perovskite crystal structure, characterized by atoms rearranged in a certain pattern, is exhibited by a class of minerals known as perovskite oxide materials [1]. The core cation is positioned at the center of each oxygen octahedron in the three-dimensional framework that makes up the perovskite structure. Perovskite oxide constituents have the common formula ABO₃, where "A" stands for a bigger cation, "B" for a smaller cation, and "O" for oxygen [2]. A broad range of elements can be used to modify the cations of A-site and B-site, giving perovskite oxides an enormous amount of flexibility. Additionally, the adjustable characteristics, excellent chemical stability, capacity to tolerate hostile conditions, plenty of element availability, opportunities for interface engineering, and prospective upcoming applications make Perovskite oxide materials stand out among exceptional materials [3]. They offer huge opportunities for scientific progress, technological innovation, and long-term fixes in a variety of disciplines, laying the foundation for an innovative and easy future. The potential of perovskite oxide materials is further highlighted by newly developed applications in a

variety of fields, including electrical devices, solid oxide fuel cells, energy storage, sensors, and catalysis [4,5].

These materials provide unique interface engineering possibilities which give them additional versatility. They can combine with other materials to generate heterostructures and interfaces, resulting in beneficial effects and improved functionality. This trait allows them to function in hybrid systems, creating new possibilities for creative device concepts and enhanced performance. The ability of perovskite oxides to alter their composition, which can be achieved by adding flaws or changing cations, is one of their main advantages [6, 7]. Further demonstrating their promise for a wide range of technological breakthroughs, these alterations enable researchers to modify the materials' characteristics to match certain application requirements. Through the application of computational methods such as DFT, scientists can obtain a crucial understanding of the functionality and act of these materials. These insights can then be used to direct experimental research and make it easier to optimize perovskite-based devices for a variety of applications, creating new opportunities for technological advancement [8-11].

Perovskite oxide materials do, however, face several significant difficulties despite their enormous potential, such as limitations in stability, moisture sensitivity, and scaling issues. To overcome these restrictions and realize the full promise of perovskite oxide for real-world applications, research is still ongoing [12, 13]. Here, we used a cutting-edge DFT approach by using the code of CASTEP, precisely applying the approximation of PBE-GGA, to investigate the effects of induced varying stress at 0, 40, 80, 120, and 160 GPa on the properties for cubical structured HfMgO_3 perovskite. This allowed us to gain comprehensive knowledge that can help advance various fields. In the published literature, we did not find any experimental and computed DFT evidence of HfMgO_3 . For the first time, we are presenting a DFT study of HfMgO_3 .

2. Computational details

The Material Studio setup is used in this study to conduct a detailed examination of the electronic, elastic, mechanical, optical, and thermal properties of HfMgO_3 .

The Cambridge Serial Total Energy Package (CASTEP) code [14, 15], which makes use of the plane wave pseudopotential approach and density functional theory (DFT) concepts, is used to carry out the complete computational analysis [16, 17]. To account for electron transfers, the generalized gradient approximation (PBE-GGA) method was introduced by the Perdew-Burke-Ernzerhof (PBE) exchange connection parameterization [18, 19]. As shown in Fig. 1(a), the GGA calculations are accomplished on a cubical structured HfMgO_3 having a pm-3m (221) space group. The supercell with magnitudes of $2 \times 2 \times 1$ with 340 eV deadline energy is used to depict the interaction of an electron with an ion by using ultrasoft pseudopotential. The plane wave functions can be used as a collection of bases to appropriately represent the electronic wave functions. The Pulay mixing process is applied for the Brillouin zone combination using the 222 k-point MPG (Monkhorst-Pack grid) [20, 21]. The self-consistent field (SCF) tolerance is fixed to 1×10^{-6} eV/atom and the band energy tolerance to 1×10^{-5} eV [22]. All the physical properties are measured by varying stress of 0, 40, 80, 120, and 160 GPa. The atomic displacement is settled at less than 0.00001 Å [23].

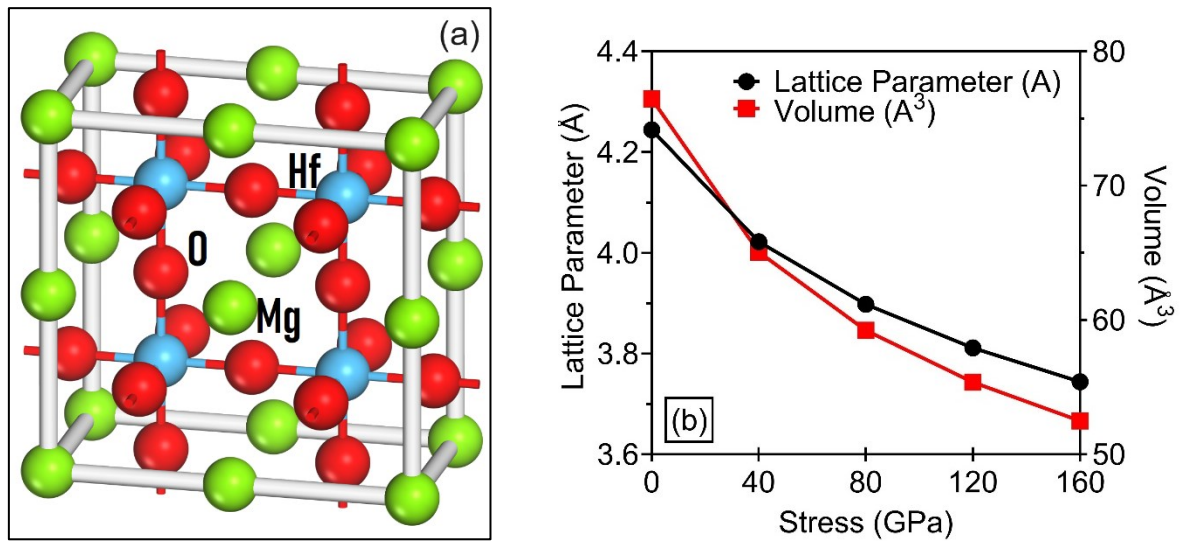


Fig. 1. (a) HfMgO_3 Supercell (b) Lattice parameter vs stress and lattice volume vs. stress (colour online)

3. Results and discussion

3.1. Electronic properties

The lattice constant “a” and cell volume “V” both are plotted with applied stress shown in Fig. 1(b). As stress increases (0, 40, 80, 120, and 160 GPa), it appears that the lattice parameter (5.86664 to 5.14887 Å) and cell size (201.91487 to 136.50098 Å^3) both decrease. This is shown in Fig. 2. The exact computation of important parameters, such as the electronic band gap, total and partial density of states (PDOS), and (TDOS), is necessary for the evaluation of electrical properties [24, 25]. The density of states explicitly and deeply illustrates the impact of s, p, d,

and f substates, in addition to their intra and inter-band evolutions in bands. In the meantime, the band gap construction provides insightful information regarding the precise role played by valence electrons from various materials.

These rigorous calculations provide for a precise and in-depth understanding of the complex electrical properties displayed by the materials under examination, permitting a thorough analysis and investigation of their possible applications in a variety of fields. The band structure of HMgO_3 is shown in Fig. 2(a–e), calculated with high regularity and tracked by $G \rightarrow F \rightarrow Q \rightarrow Z \rightarrow G$ k-points that covered from ± 4 eV. At zero photon energy, the Fermi level (E_f) was represented by a dashed line. The

data plotted in Fig. 2(f), shows an increasing trend in the band gap of HfMgO_3 from 0.442 eV to 0.757 eV with increasing stress levels from 0–40 GPa and then decreasing from 40–160 GPa indicating that higher stress levels lead to a wider band gap caused by band stretching or electron ions interactions become stronger [26]. An essential method for thoroughly examining the various facets of band structure is the use of PDOS and TDOS. The excited electrons numbers and accessible states of electrons can be calculated using Fermi's Golden Rule [27]. Furthermore, a method for determining the number of mobile states in a substance is electrical conductivity. These state-of-the-art techniques allow researchers to identify important features of electron dynamics, absorption patterns, and the mobility of charge carriers

[27, 28], providing a profound grasp of the intricate details of band structure.

The results finding of electronic band gap calculations revealed that there is a band gap rise from (0.422 – 0.757 eV) when stress is applied at 40 GPa, but on further applied stress the band gap is decreased from (0.757 – 0.589 eV). The band gap at 160 GPa was found greater than the value at 0 GPa. In analysis, the maximum value of 0.422 eV of the band gap was found at 40 GPa shown in Fig. 2(f). In HfMgO_3 direct band gap minimizes at the symmetry point. The selected material displays a maximum band gap at a load of 40 GPa, then on further increase in stress from 40 to 160 GPa the level of band gap becomes narrow as shown in Fig. 2(f).

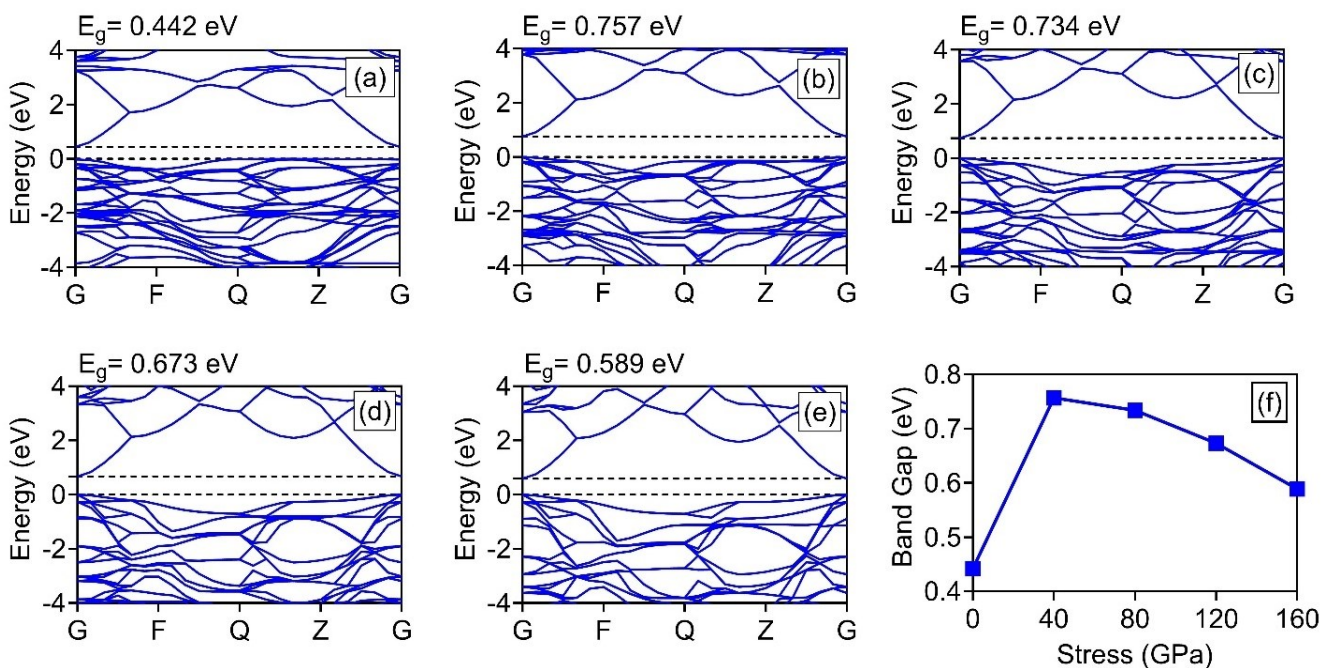


Fig. 2. (a–e) Band structure of HfMgO_3 at 0, 40, 80, 120, and 160 GPa. (f) Bandgap vs stress (colour online)

Fig. 3 represents the Total Density of States (TDOS) for HfMgO_3 from 0–160 GPa. As the external stress increases, the electronic structure of HfMgO_3 undergoes significant changes. At 0 GPa, the TDOS shows distinct peaks at lower energy levels with a noticeable band gap around 0 eV, indicating semiconductor behavior. As stress increases to 40 GPa, the band gap slightly decreases, suggesting a shift towards metallic behavior. At 80 GPa, the peaks in the TDOS broaden, and the band gap further narrows. By 120 GPa, the TDOS near the Fermi level becomes more populated, with the material exhibiting metallic characteristics as the band gap continues to reduce. At the highest stress level of 160 GPa, the TDOS shows a higher density of states near the Fermi level, indicating a minimal or non-existent band gap and a clear transition to metallic behavior. Thus, the application of external stress progressively transforms HfMgO_3 from a semiconductor to a metallic state. The findings

demonstrated that when stress is applied, the valence and conduction bands expand.

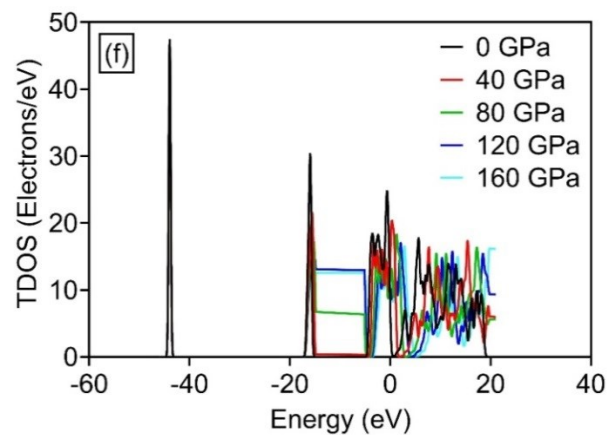


Fig. 3. TDOS of HfMgO_3 at varying stress levels (colour online)

3.2. Optical properties

Examining a substance's optical characteristics provides a thorough picture of how it interacts with the wave spectrum. To ascertain the optical features of HfMgO_3 , our study uses computational estimation to calculate the refractive index (n), reflectivity $R(\omega)$, absorption $I(\omega)$, dielectric function $\varepsilon_1(\omega)$ real and $\varepsilon_2(\omega)$ imaginary, loss function $L(\omega)$, optical conductivity $\sigma_1(\omega)$ real and $\sigma_2(\omega)$ imaginary [24, 25, 23].

$$I(\omega) = \sqrt{2}\omega \left(\sqrt{\varepsilon_1(\omega)^2 + \varepsilon_2(\omega)^2} - \varepsilon_1(\omega) \right)^{1/2} \quad (1)$$

$$K(\omega) = \frac{I(\omega)}{2\omega} \quad (2)$$

$$L(\omega) = \frac{\varepsilon_2}{(\varepsilon_1(\omega)^2 + \varepsilon_2(\omega)^2)} \quad (3)$$

$$n(\omega) = \left(\frac{1}{\sqrt{2}} \right) \left(\sqrt{\varepsilon_1(\omega)^2 + \varepsilon_2(\omega)^2} - \varepsilon_1(\omega) \right)^{1/2} \quad (4)$$

$$r(\omega) = \frac{n+iK-1}{n+iK+1} \quad (5)$$

$$\sqrt{\varepsilon(\omega)} = n(\omega) + iK(\omega) \quad (6)$$

$$\varepsilon_1(\omega) = n^2 - K^2 \quad (7)$$

$$\varepsilon_2(\omega) = 2nK \quad (8)$$

$$\varepsilon(\omega) = \varepsilon_1(\omega) + i\varepsilon_2(\omega) \quad (9)$$

In the above equations, $I(\omega)$, $\varepsilon(\omega)$, $\varepsilon_1(\omega)$, $\varepsilon_2(\omega)$, $K(\omega)$, $L(\omega)$, $n(\omega)$ and $r(\omega)$ are absorption coefficient, dielectric function, real dielectric, imaginary dielectric, extinction coefficient, function of energy, refractive index, and reflectivity coefficient.

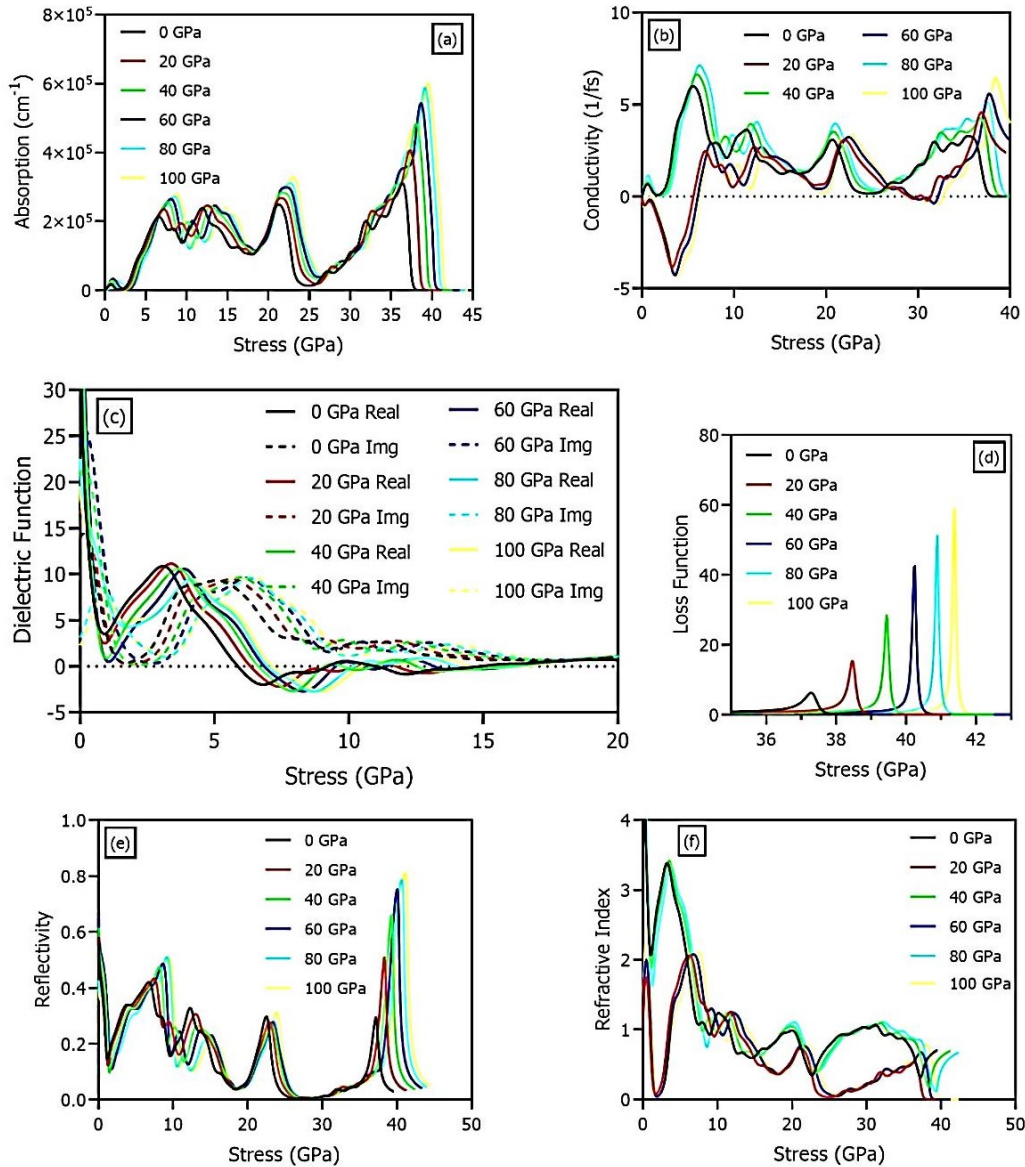


Fig. 4. Optical properties of HfMgO_3 (colour online)

The absorption spectrum for HfMgO₃ is anticipated to be at 0-160 GPa. The UV zone shown in Fig. 4 (a) contains the frequency range from 65 to 72 eV, where absorption is maximum. In this instance, the material's ability to store energy is also increased. The material that was finally chosen has applications in optoisolators, photomultipliers, UV image devices, photoresistors, photodiodes, and photoconductive devices for cameras, among other optoelectronic devices. Fig. 4 (b) depicts the conductivity of HfMgO₃. It can be observed how stress values affect conductivity values here; as energy levels rise above 58 eV, conductivity is increased to maximum height. The dielectric function is shown in Fig. 4 (c). The highest value of dielectric constant or static dielectric is 34.78 which is found at 0 eV for 40 GPa, and it was found at 10.7 for 0 GPa. The energy loss function $L(\omega)$ of HfMgO₃ at diverse stress values, 0, 40, 80, 120, and 160 GPa is also expected revealed in Fig. 4(d). The maximum value of the loss function is found at 64.17 for 0 GPa. Peaks in the energy loss function correspond to collective oscillations of electrons inside the material and on the surface, known as plasmons. Furthermore, this energy loss is due to the excitation of electrons due to photon interaction and scattering of photons when they interact with electrons.

Computer modeling is also used to forecast the reflectance of HfMgO₃ for applied loads that vary from 0 to 160 GPa. The highest level of reflectance is seen for 160 GPa. Generally, the refractive index has two parts: an imaginary part ("k") and a real part ("n"). Its imaginary component specifies how much light at a specific wavelength is captured by the substance, but its real component specifies how quickly light passes through the substance. The real refractive index is plotted with frequency in eV, as shown in Fig. 4(f). According to our findings, the refractive index is close to 2.2.

3.3. Elastic and mechanical properties

It is achievable to analyze a material's properties, including stiffness and stability by determining the elastic constants [29]. C_{11} , C_{12} , and C_{44} are the three foremost elastic constants for a cubical crystalline structure. Fig. 5 represents the relation between elastic coefficients and applied stress. The coefficient C_{12} offers information on the contrary growth of materials, which is even found to rise from 0 to 80 with the rise in stress. When the stress increases from 0 to 80 GPa, the shear stress indicated by coefficient C_{11} increases from 371.1804 to 1189.9768. For a cubical structure, the basic stability requirements are $C_{11}-C_{12} > 0$; $C_{11} > 0$; $C_{44} > 0$; $C_{11} + 2C_{12} > 0$; $C_{12} < B < C_{11}$ [23].

The material confirms cubic stability up to 80 GPa due to its agreement with the requisite stability parameters. Beyond this stress barrier, the elastic constant C_{44} changes, and the cubic stability is lost by the material. To conclude the firmness or stability of HfMgO₃, fundamental mechanical properties like (Young's, bulk, shear) moduli denoted by (E, B, G), anisotropic factor (A), (Poisson's,

Pugh's) ratio's denoted by (ν, σ) respectively [31] and Cauchy pressure (C_P) are calculated.

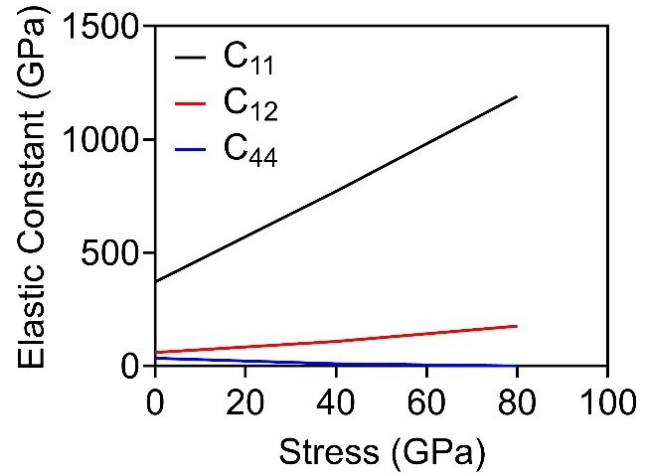


Fig. 5. C_{11} , C_{12} , and C_{44} elastic constants plotted with applied stress (colour online)

Each of the aforementioned parameters is computed by summing the results of the elastic constant calculations of the pertinent equations [30, 24, 31, 32];

$$E = \frac{9GB}{3B + G} \quad (10)$$

$$\nu = \frac{3B - G}{2(3B + G)} \quad (11)$$

$$G_V = \frac{1}{5}(3C_{44} + C_{11} - C_{12}) \quad (12)$$

$$G_R = \frac{5(C_{11} - C_{12})C_{44}}{3(C_{11} - C_{12}) + 4C_{44}} \quad (13)$$

$$G = \frac{G_V + G_R}{2} \quad (14)$$

$$B_V = B_R = \frac{C_{11} + 2C_{12}}{3} \quad (15)$$

$$B = \frac{B_V + B_R}{2} \quad (16)$$

$$P_C = C_{12} - C_{44} \quad (17)$$

$$A = \frac{2C_{44}}{C_{11} - C_{12}} \quad (18)$$

The rising Young's, shear, and bulk moduli (180 to 260, 80 to 95, and 150 to 550, respectively) are plotted against the applied stress range (0 to 80 GPa) in Fig. 6(a).

The Frantsevich ratio (G/B) [33] is also calculated for HfMgO₃ and all values are less than 0.5. According to our research, HfMgO₃ is ductile below the considered stress

values, from 0–80 GPa represented in Fig. 6(b). The anisotropic nature is illustrated by another estimate that is shown in the same graph. Equation (18) produces the anisotropic part A. If $A = 1$, the material is anisotropic; if not, it is isotropic [34]. Another important mechanical parameter that evaluates brittleness or ductility is the Poisson's ratio (ν). When the ratio is less than 0.26, it exposes a brittle nature, and when the ratio is greater than 0.26, it shows a covalent or ductile nature [35]. According to our anticipated findings, HfMgO_3 is found to be ductile, as depicted in Fig. 6(b).

Pugh's ratio measures the bulk-to-shear moduli of a material to assess its plastic properties, such as its brittleness and ductility [28, 36]. If the ratio is greater than

1.75, the selected substance would be ductile; if not, it becomes brittle. The selected material HfMgO_3 showed ductile behavior at all stress ranges between 0 and 80 GPa, as displayed in Fig. 6(c). Cauchy pressure (C_p) [37], further clarifies brittle and ductile characteristics, as shown in Fig. 6(d). The brittleness or ductility is determined by the Cauchy pressure (C_p). Ductility is indicated by a positive C_p . The compound is ductile at all stress conditions from 0–80 GPa, according to the HfMgO_3 projected DFT results because the C_p is positive under all stress conditions. Furthermore, it should be mentioned that when stress levels increase, so do the values of (C_p).

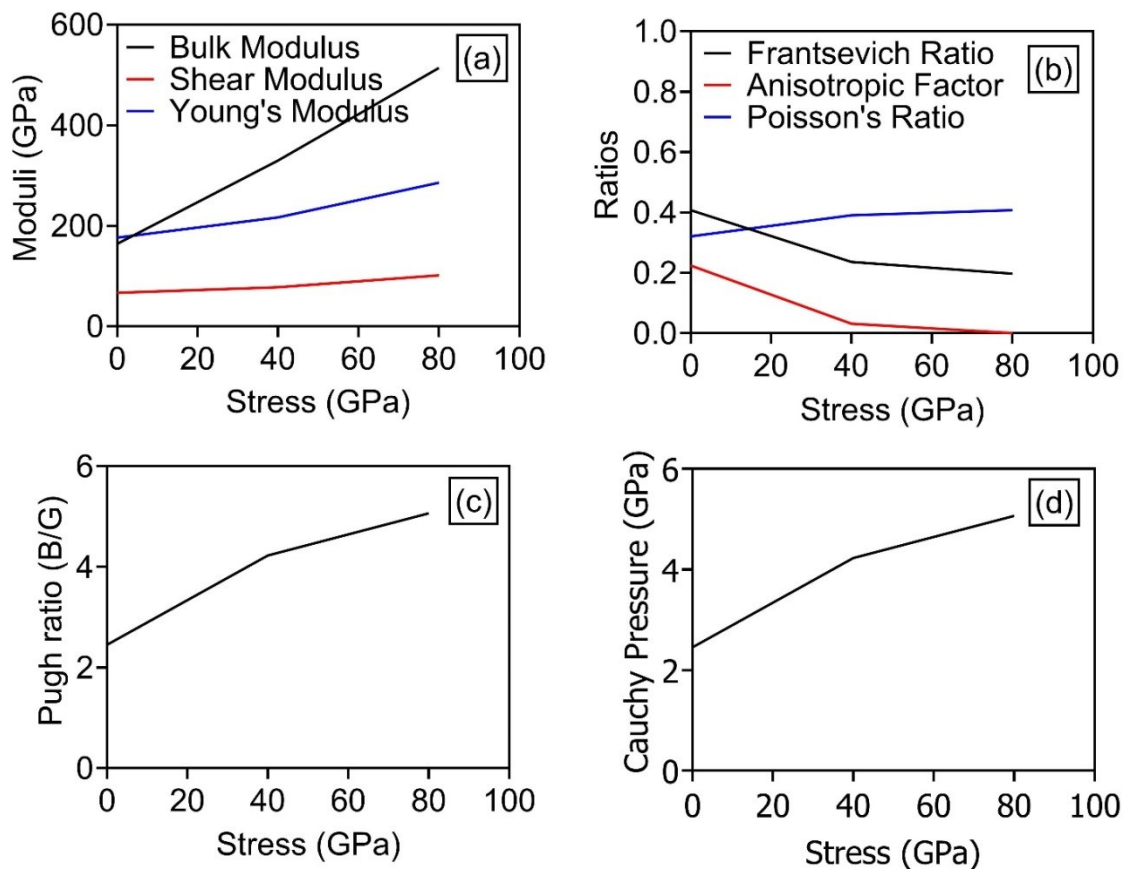


Fig. 6. Elastic and mechanical properties of HfMgO_3 (colour online)

3.4. Thermodynamic properties

The equation given below gives the total translational, rotational, vibrational, and electronic energy of a molecule [29].

$$E = E_t + E_r + E_v + E_e \quad (19)$$

In our study, we estimated the thermodynamic parameters like Debye temperature, enthalpy, heat

capacity, free energy, and entropy with varying stress 0–160 GPa shown in Fig. 7 (a–e).

From Fig. 7(a), the enthalpy value is greatest at 0 GPa. The same result patterns observed for entropy, and heat capacity values are shown in Fig. 7(c & d). However, as illustrated in Fig. 7(b), free is highest for 160 GPa, and for Debye temperature, it was found also highest represented in Fig. 7(e).

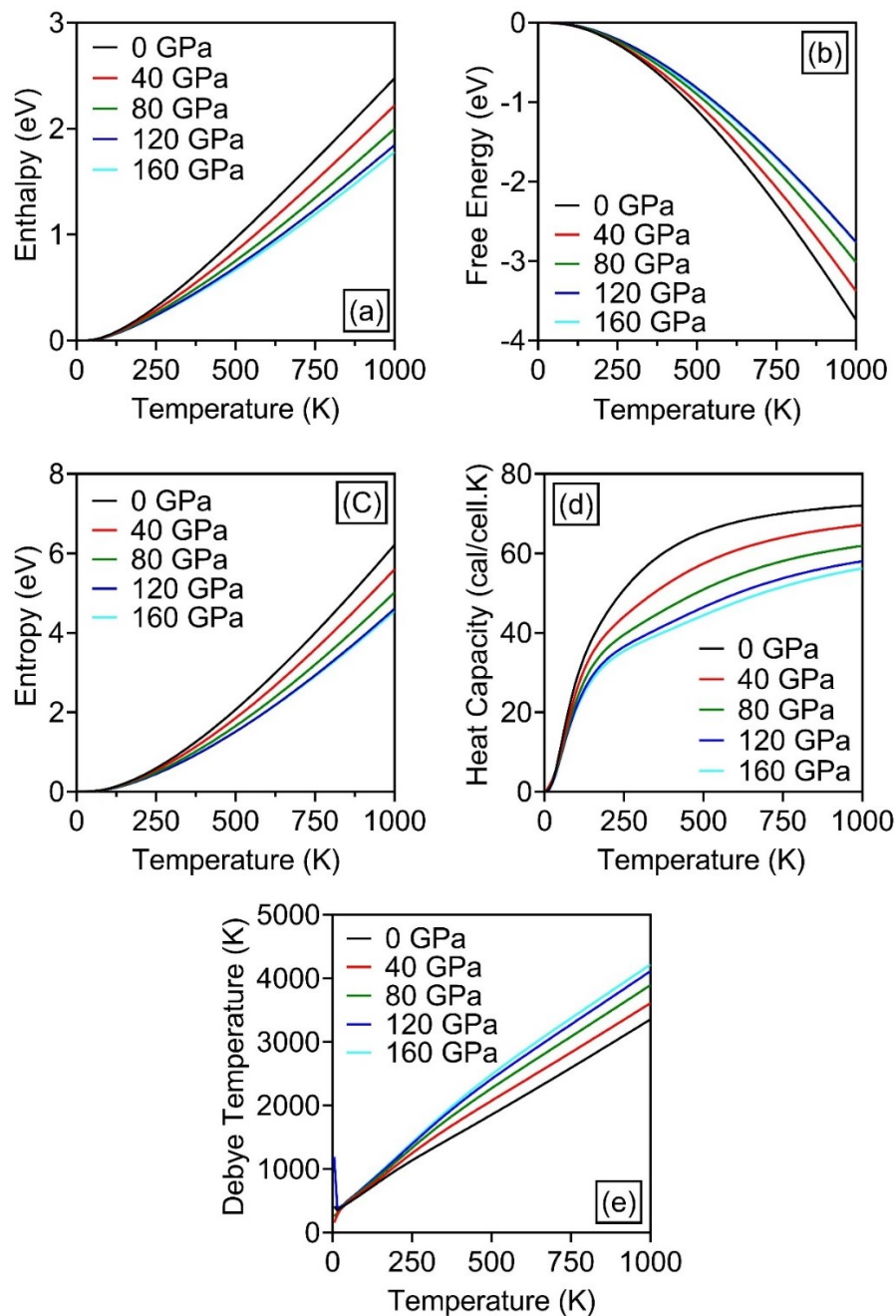


Fig. 7. Thermodynamic characteristics (colour online)

As shown in Fig. 9 (a–e), the computational predictions of the phonon dispersion for HfMgO_3 under dissimilar stress stages of 0, 40, 80, 120, and 160 GPa are also calculated. Here, It is visible that the spreading of phonons exhibits a variety of frequency modes, specifically imaginary modes, indicating that there may be an unstable cubic phase at 0 K. Peijun Guo et al. [38] derived the same type of analyzed result for HfMgO_3 at 0 GPa. The dispersion of the phonons at 40 GPa exhibits a clear gap, as illustrated in Fig. 9(b). The phonon gap

widens with increasing stress values up to 160 GPa. Noticeably in Fig. 8(a–d) the rise in stress value from 0–160 GPa, the range is expanding for imaginary modes of phonons frequencies. One can readily see maximum dispersion at 160 GPa. The same behavior was seen for DOS vs. freq plot in Fig. 8(e). The frequency range for both imaginary and real modes was seen greater at higher stress values.

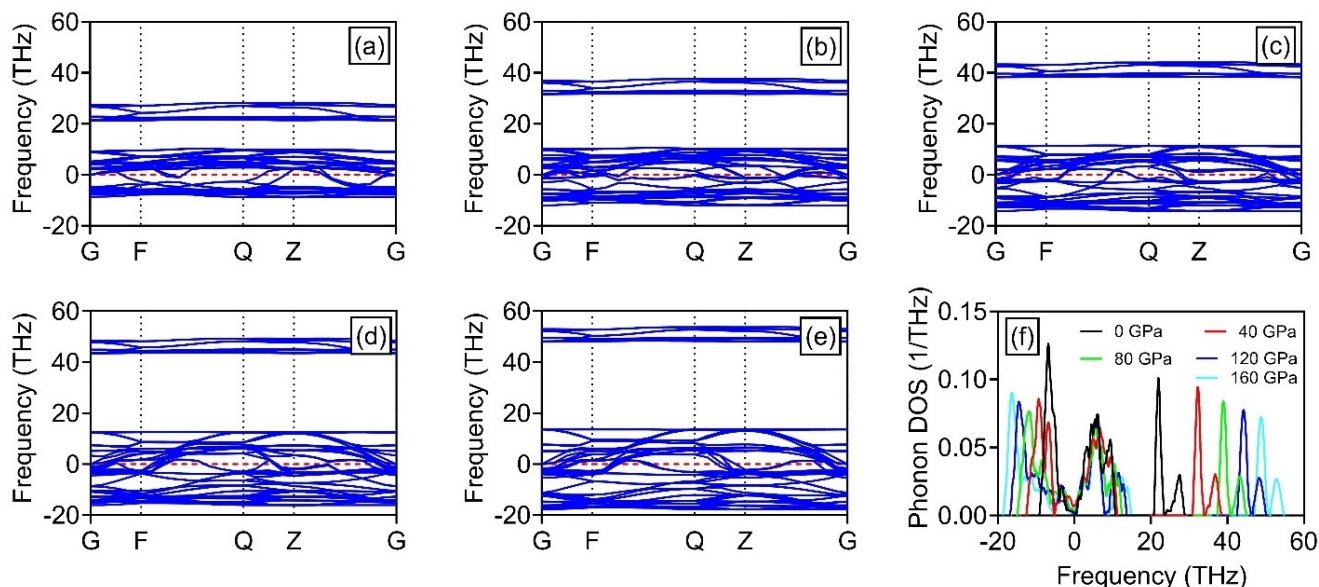


Fig. 8. Phonon dispersion at 0 Kelvin at (a) 0 GPa, (b) 40 GPa, (c) 80 GPa, (d) 120 GPa, (e) 160 GPa, and (f) Density of Phonon states vs frequency for HfMgO_3 (colour online)

4. Conclusion

The GGA-PBE is used for first-principles simulation calculations to ensure that HfMgO_3 has the best optical and electronic attributes. The lattice parameters ranging from 201.91487 to 136.50098 Å, and lattice volume from 5.86664 to 5.14887 Å³ are predicted through simulation findings. The results of the band gap measurements presented that as the stress increased, the computed band gap values likewise increased, reaching their maximum at 40 GPa, and subsequently the band decreased as the stress proceeded further. Up to 80 GPa, this compound is cubically stable and shows instability at 120 GPa and onwards. According to the information from our PDOS approximated calculations, upper valence band creation is caused by Oxygen and Magnesium p-states, whereas lower conduction band creation is caused by p-states of magnesium and d-states of Hafnium. Similar to how Magnesium's p-state dominates for the lower valence band almost at 44 eV, Oxygen's s-state contributes most to the creation of the mid-valence band under all stress circumstances. Similar peak behavior of states was observed for all stress settings. In the cubic phase (Pm-3m), which exhibits the movement of absorption peaks toward higher energies, the results of the optical characteristics were also thoroughly examined. The maximum value of absorption is 72 eV. According to the calculations, the static dielectric function is 34.78. As a result, this material can be used in electro-optical devices.

Acknowledgement

The authors extend their appreciation to Taif University, Saudi Arabia, for supporting this work through project number (TU-DSPP-2024-321).

Funding

This research was funded by Taif University, Taif, Saudi Arabia, Project No. (TU-DSPP-2024-321).

References

- [1] A. Kumar, A. Kumar, V. Krishnan, *ACS Catalysis* **10**(17), 10253 (2020).
- [2] A. Žužić, A. Ressler, J. Macan, *Ceramics International* **48**, 35947 (2022).
- [3] R. J. H. Voorhoeve, D. W. Johnson, J. P. Remeika, P. K. Gallagher, *Science* **195**, 827 (1977).
- [4] A. Žužić, V. Filipan, I. Sutlović, J. Macan, *Technical Gazette* **29**(4), 1419 (2022).
- [5] C. A. Hancock, J. M. Porras-Vazquez, P. J. Keenan, P. R. Slater, *Dalton Transactions* **44**, 10559 (2015).
- [6] F. Mahmoudi, K. Saravanakumar, V. Maheskumar, L. K. Njaramba, Y. Yoon, C. M. Park, *Journal of Hazardous Materials* **436**, 129074 (2022).
- [7] C. Sun, J. A. Alonso, J. Bian, *Advanced Energy Materials* **11**(2), 2000459 (2021).
- [8] J. Varignon, M. Bibes, A. Zunger, *Nature Communications* **10**, Article number: 1658 (2019).
- [9] M. M. Saad H.-E., A. Elhag, *Results in Physics* **9**, 793 (2018).
- [10] J. Munir, M. Khuram Iftikhar, M. Imran Jamil, Moeen Ud Din, *Physica Scripta* **98**(6), 065513 (2023).
- [11] S. Zhao, Z. Wei, S. A. Dar, *Zeitschrift für Naturforsch. - Sect. A J. Phys. Sci.* **74**(9)a, 827 (2019).
- [12] S. Aperi, C. Koch, G. Brocks, S. Olthof, S. Tao, *ACS Applied Materials and Interfaces* **14**(30), 34208 (2022).

- [13] L. Yang, Y. Li, Y. Sun, W. Wang, Z. Shao, *Energy and Environmental Materials* **5**(3), 751 (2022).
- [14] S. J. Clark, Matthew D. Segall, Chris J. Pickard, Phil J. Hasnip, Matt I. J. Probert, Keith Refson, Mike C. Payne, *Zeitschrift für Kristallographie - Crystalline Materials* **220**, 567 (2005).
- [15] A. H. Mazurek, Ł. Szeleszczuk, D. M. Pisklak, *Pharmaceutics* **12**(5), 415 (2020).
- [16] M. Bouchenafa, Y. Bourourou, A. Khelefhom, H. Boulebdia, M. A. Fadla, A. Benmakhlouf, S. Maabed, M. Halit, M. Sidoumou, *Computational Condensed Matter* **30**, e00644 (2022).
- [17] M. A. Fadla, B. Bentría, T. Dahame, A. Benghia, *Physica B: Condensed Matter* **585**, 412118 (2020).
- [18] M. Ernzerhof, G. E. Scuseria, *J. Chem. Phys.* **110**(11), 5029 (1999).
- [19] H. M. Ghaithan, Z. A. Alahmed, A. Lyras, S. M. H. Qaid, A. S. Aldwayyan, *Crystals* **10**(5), 342 (2020).
- [20] Y. Wang, P. Wisesa, A. Balasubramanian, S. Dwaraknath, T. Mueller, *Computational Materials Science* **187**, 110100 (2021).
- [21] P. Wisesa, K. A. McGill, T. Mueller, *Phys. Rev. B* **93**, 155109 (2016).
- [22] C. Ming, H. Wang, D. West, S. Zhang, Y. Y. Sun, *J. Mater. Chem. A* **10**, 3018 (2022).
- [23] M. I. Khan, S. M. J. Zaidi, M. S. U. Sahar, S. S. A. Gillani, M. A. Qaisrani, M. U. Farooq, *J. Electron. Mater.* **52**(8), 5631 (2023).
- [24] S. M. J. Zaidi, M. I. Khan, S. S. A. Gillani, M. S. U. Sahar, S. Ullah, M. Tanveer, *Mater. Res. Express* **9**(12), 125501 (2022).
- [25] M. Rizwan, Zahid Usman, Muhammad Shakil, S. S. A. Gillani, S. Azeem, H. B. Jin, C. B. Cao, Rana Farhat Mehmood, Ghulam Nabi, Muhammad Adnan Asghar, *Mater. Res. Express* **7**(1), 015920 (2020).
- [26] G. Murtaza, G. Sadique, H. A. Rahnamaye Aliabad, M. N. Khalid, S. Naeem, A. Afaq, B. Amin, Iftikhar Ahmad, *Physica B: Condensed Matter* **406**(24), 4584 (2011).
- [27] H. Arshad, M. Zafar, S. Ahmad, M. Rizwan, M. I. Khan, S. S. A. Gillani, Chuan Bao Cao, M. Shakil, *Mod. Phys. Lett. B* **33**(31), 1950389 (2019).
- [28] M. Rizwan, Waqar Azam, S. S. A. Gillani, I. Zeba, M. Shakil, S. S. Ali, Riaz Ahmad, *Molecular Physics* **119**(9), e1892226 (2021).
- [29] A. Abdullah, S. M. J. Zaidi, M. I. Khan, M. S. U. Sahar, A. S. Saleemi, *Comput. Condens. Matter* **35**, e00804 (2023).
- [30] M. I. Khan, S. M. J. Zaidi, M. S. U. Sahar, S. S. A. Gillani, M. A. Qaisrani, M. U. Farooq, *Journal of Electronic Materials*, **52**, 5631, (2023)
- [31] M. Shakil, H. Sadia, M. I. Khan, S. S. A. Gillani, M. A. Gadhi, I. Boukhris, *Physica B: Condensed Matter* **625**, 413524 (2022).
- [32] M. Shakil, H. Sadia, I. Zeba, S. S. A. Gillani, S. Ahmad, M. Zafar, *Solid State Commun.* **325**, 114157 (2021).
- [33] S. M. J. Zaidi, M. I. Khan, S. S. A. Gillani, M. S. U. Sahar, S. Ullah, and M. Tanveer, *Mater. Res. Express* **9**(12), 125501 (2022)
- [34] M. Shakil, A. Akram, I. Zeba, R. Ahmad, S. S. A. Gillani, M. A. Gadhi, *Mater. Res. Express* **7**(2), 025513 (2020).
- [35] S. S. A. Gillani, A. Ejaz, M. Shakil, Tousif Hussain, Riaz Ahmad, Muhammad Rafique, Waris Ali, Khurram Shahzad, Arshad Mahmood Ali, *Optik* **241**, 167024 (2021).
- [36] M. Rizwan, Rabia Bibi, Tariq Mahmood, Imran Aslam, Syed Sajid Ali Gillani, Hai Boa Jin, Chuan Bao Cao, Zahid Usman, Ahmad Maqsood, *EPJ Appl. Phys.* **88**(1), 10501 (2019).
- [37] I. Ilyas, A. A. Zafar, H. M. Naeem Ullah, M. Rizwan, Z. Usman, S. S. A. Gillani, *J. Phys. Chem. Solids* **165**, 110642 (2022).
- [38] P. Guo, Yi Xia, Jue Gong, Constantinos C. Stoumpos, Kyle M. McCall, Grant C. B. Alexander, Zhiyuan Ma, Hua Zhou, David J. Gosztola, John B. Ketterson, Mercouri G. Kanatzidis, Tao Xu, Maria K. Y. Chan, Richard D. Schaller, *ACS Energy Lett.* **2**(10), 2463 (2017).

*Corresponding author: ijazkhan4123@gmail.com